Volume 7
Number 21
7 November 2025
Pages 6663–7050

Nanoscale Advances

rsc.li/nanoscale-advances

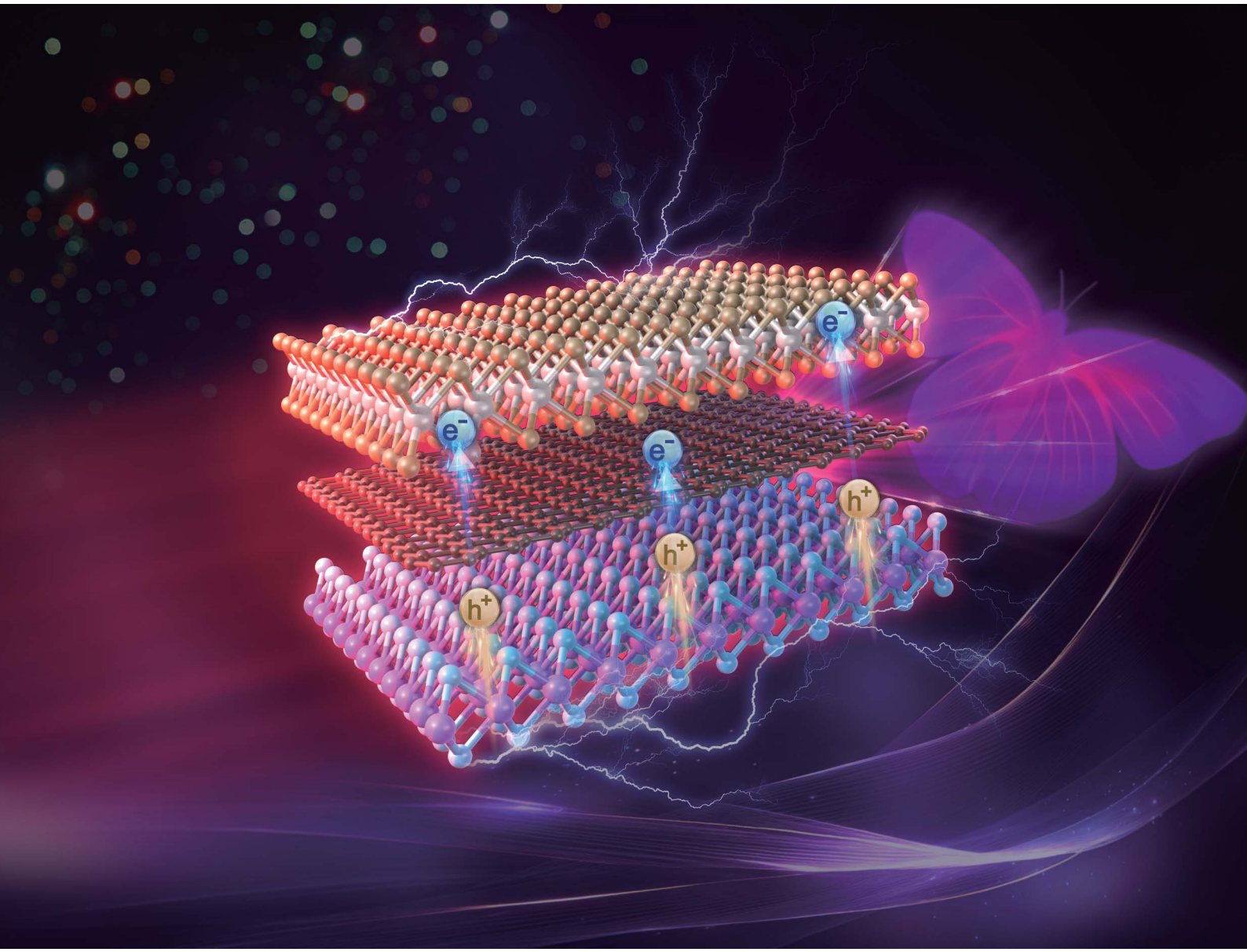

ISSN 2516-0230

ROYAL SOCIETY OF CHEMISTRY

PAPER
Zichao Ma and Changjian Zhou
Electrostatically enhanced infrared absorption in two-dimensional van der Waals structures

NCNST

Nanoscale Advances

ROYAL SOCIETY OF CHEMISTRY

PAPER

View Article Online
View Journal | View Issue

Cite this: *Nanoscale Adv.*, 2025, **7**, 6819

Electrostatically enhanced infrared absorption in two-dimensional van der Waals structures

Zichao Ma and Changjian Zhou *

Two-dimensional (2D) semiconductors exhibit strong light absorption, yet their large bandgaps limit broadband photodetection. While van der Waals (vdW) heterostructures of 2D materials enable infrared excitation through narrowed interlayer bandgaps, achieving efficient control over these interlayer transitions remains a fundamental challenge. Through first-principles simulations and electrostatic engineering approaches, this study establishes a direct correlation between interfacial charge redistribution and enhanced interlayer excitations in 2D vdW structures. The results demonstrate that versatile strategies such as external electric field application, substitutional doping, and graphene interlayer integration effectively reduce interlayer bandgaps by several hundred millielectronvolts while significantly increasing interfacial charge exchange. These engineered heterostructures achieve exceptional absorption coefficients greater than 10^5 cm^{-1} spanning visible to mid-infrared wavelengths. These findings provide essential design principles and offer engineering strategies for developing broadband photodetectors using 2D vdW structures.

Received 2nd July 2025
Accepted 4th September 2025

DOI: 10.1039/d5na00648a

rsc.li/nanoscale-advances

1 Introduction

Two-dimensional (2D) semiconductors exhibit exceptional light–matter interaction and high carrier mobility within their ultrathin atomic layers, making them attractive for photodetectors that demand both high sensitivity and rapid response.[1,2] Strong photon absorption across a broad spectral range underpins high-performance photodetection at the nanoscale.[3] Vertically stacked heterostructures formed through van der Waals (vdW) assembly of 2D layered materials present several unique advantages for photodetection applications,[4] including atomically sharp interfaces, freedom from lattice-matching constraints, and tunable band alignment properties. These features collectively enable enhanced photodetector performance in the visible spectrum, as demonstrated by high responsivities,[5] fast response speed,[6] low dark current, and self-powered operation.[7]

Typically, vdW structures assembled from 2D materials with differing bandgaps exhibit a staggered (type-II) band alignment. This configuration facilitates charge transfer across the atomically sharp junctions and induces built-in electric fields influencing carrier dynamics.[8,9] In such heterostructures, the interlayer bandgap can be several hundred millielectronvolts (meV) smaller than the intrinsic bandgaps of the constituent monolayer. This reduced optical bandgap has enabled interlayer exciton recombination and subsequent infrared photon emission through ultrafast excitonic processes at cryogenic temperatures, for example, in heterostructures consisting of large bandgap $MoSe_2$ and WSe_2 when pumped with green lasers.[10–13] In contrast, interlayer absorption as a reverse process, where an incoming photon excites electron–hole pairs spatially separated in two 2D layers, encounters significant inefficiency challenges. Such excitonic absorptions require extremely high incident light intensities, often exceeding 10^{10} W cm^{-2}, which are orders of magnitude greater than typical photodetector operating conditions (nW cm^{-2} to mW cm^{-2}).[14] This stark contrast in light intensity illustrates the severe inefficiency of exciton-mediated interlayer-bandgap absorption for high-performance infrared photodetection applications.

Furthermore, excitonic effects in 2D materials, which are typically weakly bound and require cryogenic operating temperatures, contribute to sub-bandgap absorption only about 0.1 eV below the band edge. Given that most 2D semiconductors have bandgaps between 1 and 2 eV, this limited spectral extension, combined with the stringent excitation conditions, makes excitonic mechanisms impractical as an engineering route for high-performance photodetection device applications. As a result, the absorption spectra of 2D vdW heterostructures remain largely confined to the visible and near-infrared range, and practical strategies to extend absorption threshold into the mid-infrared *via* interlayer excitons have seen limited progress.[15–17]

These fundamental limitations highlight the need for alternative approaches, such as band engineering through a combined heterostructure design and electrostatic modulation. This makes the strategic design and control of the

School of Microelectronics, South China University of Technology, Guangzhou, 511442, China. E-mail: zhoucj@scut.edu.cn

electronic structure of 2D vdW heterostructures essential for achieving tunable and efficient absorption beyond the limitations of intrinsic excitonic processes. Furthermore, efficient interlayer tunneling and momentum conservation are essential for strong interlayer excitations,[18,19] which in turn are vital for high-response photodetection. However, many existing studies rely on multilayer 2D materials with indirect bandgaps, which suffer from momentum mismatch and reduced quantum yield.[20,21] Moreover, their small bandgaps can lead to significant dark current, thereby degrading the sensitivity and signal-to-noise ratio of the photodetector. Moreover, exploring different 2D material combinations alone remains challenging because few materials simultaneously offer transparent tunneling barriers and narrow bandgaps, both of which are critical for efficient infrared photon absorption *via* interlayer excitons. To address these gaps, researchers have turned to interface dielectric engineering and gate biasing to tailor optical responses.[22–25] In particular, interfacial electric fields have emerged as a key lever for boosting photocarrier separation, underscoring the intimate link between interface electrostatics and optical absorption in 2D vdW heterostructures.

This paper adopts a band-structure-based derivation of the absorption process to examine how band structures and interface electrostatics deterministically influence infrared optical absorption in vdW structures composed of well-established 2D monolayer materials for photodetector applications. Through first-principles simulations, this study demonstrates that deliberate tuning of the band alignment effectively modulates interlayer excitations, thereby enabling efficient infrared absorption. In particularly, the work examines the impact of electric biasing and doping on regulating the band alignment and interlayer excitation in 2D vdW structures, providing device engineering strategies to optimize infrared absorption for high-performance photodetection applications.

2 Band alignment and optical absorption of 2D vdW heterostructures

Band diagrams are essential for understanding the electronic and optical transition properties of semiconductor devices. Key features such as the conduction band minimum (E_C), valence band maximum (E_V), and the Fermi level (E_F) provide insights into barrier distribution and carrier dynamics. In contrast to bulk junctions, vdW junctions assembled from atomically thin 2D layers exhibit negligible band bending. Instead, their band alignment is set directly by interfacial charge transfer, yielding electrostatic and optical properties that differ markedly from those of isolated monolayers. To accurately capture the charge redistribution and its impact on band alignment, this work correlated the first-principles simulation results, including the band structure, projected density of states (DoS), and localized DoS, with a common energy axis to construct the band diagrams of each 2D vdW heterostructure and calibrate the bandgap and band alignment properties with those reported in the literature.[9,17]

Without loss of generality, the electronic structures of a MoS_2/WSe_2 vdW structure are investigated as a representative example. Fig. 1(a) displays the relaxed atomic structure. The vdW gap or interlayer distance, measured between the centers of interfacial Se_1 in WSe_2 and S_2 in MoS_2 atoms, is 3.72 Å, while the separation between the Mo and W atom centers is 7.05 Å. Fig. 1(b) presents the band structure, projected DoS spectrum, and localized DoS mapping for the MoS_2/WSe_2 heterostructure. The results reveal a distinct direct bandgap at the high-symmetry *K*-point of the vdW structure, with E_C originating from the MoS_2 layer and E_V from the WSe_2 layer. The spatial separation of conduction and valence bands arises from a staggered-gap alignment and results in a reduced energy gap of the vdW heterostructure for interlayer excitons.[26]

Notably, the energy levels at which the DoS of transition metal atoms (Mo and W) diminish correspond to E_C and E_V, indicating bandgap values of 1.78 eV for monolayer WSe_2 and 1.66 eV for monolayer MoS_2, in good agreement with experimental results.[17] The tunnelling layer between MoS_2 and WSe_2, identified as the interfacial dark gap in the localized DoS map, has a thickness of 1.56 Å. This region contains no allowed states and forms a tunnelling barrier that impedes interlayer charge transfer and exciton transitions, which is a universal feature in vdW structures, typically 1.5 Å to 2 Å wide.[27] These values are consistent with experimental measurements reported in high-resolution TEM studies of the MoS_2/WSe_2 heterostructure,[28] validating the computational model.

Several 2D materials used for photodetection applications, including MoS_2, WS_2, WSe_2, InSe, NbS_2, and graphene, in the form of free-standing monolayers as well as combined double-layer and triple-layer vdW structures, were simulated in this work. The lattice parameters for the unit cells are listed in Table 1. As shown in Fig. 1(c), the band diagrams of various 2D vdW heterostructure combinations alongside those of their free-standing monolayers, with calculated energy levels and band alignments consistent with the literature.[9,17] All atomic structures were initially acquired from well-established databases (**https://www.materialsproject.org**) and subsequently rescaled to specific unit cell configurations, with each undergoing lattice constant adjustments of less than 2.5%. For structure modeling, periodic boundary conditions were applied to simulate an extended 2D film, and a vacuum layer exceeding 20 Å was implemented along the *z*-axis (out-of-plane direction) for every simulation unit cell to inhibit inter-cell charge exchange.

The supercells were relaxed using first-principles molecular dynamics with the conjugated gradient method, achieving an energy convergence of 10^{-6} eV and a force convergence of 0.02 eV $Å^{-1}$. Self-consistent field (SCF) calculations were conducted using the projector-augmented wave (PAW) method with the Perdew–Burke–Ernzerhof (PBE) exchange and correlation functional within the generalized gradient approximation. A gamma-centered *k*-point grid was adopted for SCF calculations. To further confirm the band alignment of the 2D vdW heterostructures, we additionally verified our simulation results by calculating the band structures using the hybrid functional HSE06, with the results shown in supplementary Fig. S1. These

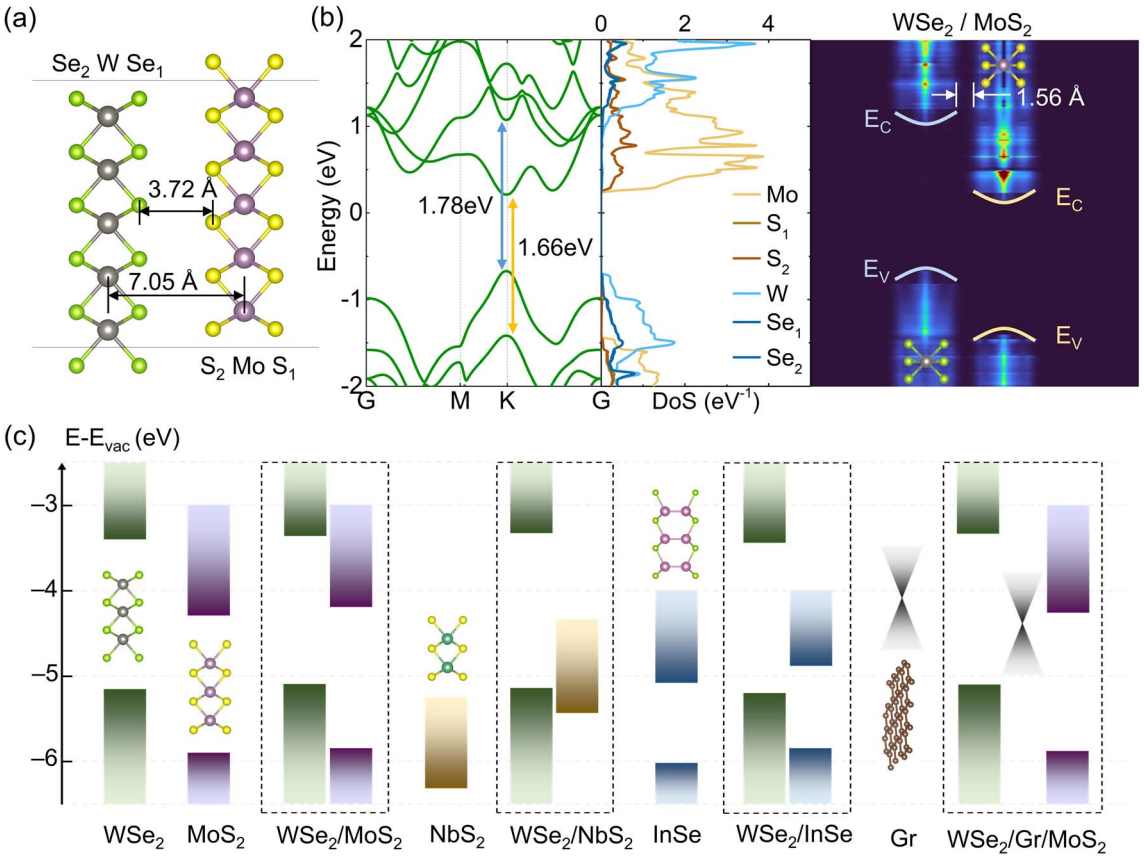

Fig. 1 (a) Atomic structure of the MoS_2/WSe_2 bilayer vdW junction. (b) The band structure, projected DoS spectrum, and localized DoS distribution of the MoS_2/WSe_2 vdW structure simulated in this work. (c) The simulated band alignment diagrams for the vdW heterostructure comprised widely studied 2D materials.

Table 1 Lattice constants and *k*-point grids used for the simulation unit cells of 2D vdW structures

Atomic structures	MoS_2/WSe_2	NbS_2/WSe_2	$InSe/WSe_2$	$MoS_2/Gr/WSe_2$
	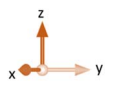	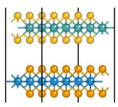	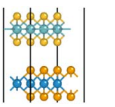	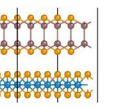
Lattice constant (Å)	9.708	6.636	16.485	9.558
k-point grids	8 × 8 × 1	12 × 12 × 1	6 × 6 × 1	9 × 9 × 1

simulations were performed using DS-PAW and Nanodcal software developed by Hongzhiwei Technology.[29]

The simulation results reveal that most vdW structures exhibit staggered band alignments, with energy level shifts relative to their free-standing forms. For example, the conduction band offset in WSe_2/MoS_2, WSe_2/InSe, and WSe_2/NbS_2 bilayer heterostructures is reduced by tens to hundreds of meV compared to that of the free-standing monolayers, which is evidence of a built-in potential at the junction interface. When two atomically thin layers come into contact, their Fermi levels equilibrate through charge transfer or charge screening, creating an interfacial dipole. This redistributed charge alters the Coulomb interaction between layers, directly tuning the interlayer coupling strength. The magnitude of charge transfer is set by the Fermi-level shift (ΔE_F) between the constituent layers in their free-standing forms and their coupled forms in the vdW heterostructure. These energy potential variations are quantitatively comparable to the first-principles simulation results. These findings demonstrate that charge exchange governs interlayer interaction strength in 2D vdW systems, with the degree of coupling determined by the initial Fermi level alignment of the constituent monolayers.

To clarify this mechanism, this work explicitly compares the $InSe/WSe_2$ and NbS_2/WSe_2 structures, which exhibit staggered-

gap (type-II) and broken-gap (type-III) band alignments, respectively. Fig. 2(a) and (d) display the changes in effective potential (ΔV_{eff}) and redistribution of charge density ($\Delta\rho$) in the constituent 2D layers of the vdW junction. The InSe/WSe_2 heterostructure, composed of two 2D monolayers with closely matched charge neutrality levels, exhibits a weak interfacial dipole, suggesting suppressed interlayer charge exchange. In contrast, the NbS_2/WSe_2 heterostructure exhibits a pronounced interfacial dipole that generates a large built-in potential, shifting the conduction band of NbS_2 upward by approximately 0.9 eV, resulting in p-type doping of the WSe_2 layer.

The linear potential drop across the vacuum region of the unit cell arises as a secondary effect of charge redistribution within the 2D heterostructure, and it follows Poisson's equation. For instance, in the WSe_2/NbS_2 heterostructure, charge transfer leads to accumulated positive charge in WSe_2 and negative charge in NbS_2, and such charge density can penetrate through the monolayers and cause residue charge density on the top and bottom surface of the vdW structure. Due to the use of periodic boundary conditions in all spatial directions in simulation, the residue negative charges in NbS_2 generate an electric field that extends across the vacuum region, terminating at the residue positive charges in WSe_2 in neighboring unit cells. To aid understanding, we have included in the supplementary document an illustration of the periodic boundary conditions used in the atomistic simulations, along with a schematic showing the redistributed charges, the induced electric field, and the resulting changes in the potential profile, presented as supplementary Fig. S2. Since the vacuum region contains no free charges, the electric field remains constant within it. Notably, because of the thick (>20 Å) vacuum spacer, this electric field does not cause significant dielectric screening or perturb the intrinsic electronic structure of the vdW heterostructures.

These interlayer interactions are further illustrated in the band structures presented in Fig. 2(b) and (e). The band structures, projected onto WSe_2, InSe, and NbS_2 (colored in blue, yellow, and orange), reveal significant joint dispersion relations near the high-symmetry Gamma-point in both heterostructures. These correlated *E-k* dispersion relations provide additional paths for momentum-conserved carrier exchange and interlayer excitations. For example, the NbS_2/WSe_2 heterostructure not only supports the interband transition of WSe_2 from E_V to E_C, but also creates an interlayer excitation pathway at the high-symmetry *K*-point, from the E_V of WSe_2 to the conduction band levels of NbS_2. A similar effect is observed for the InSe/WSe_2 heterostructure. The interband transitions occur inherently within monolayer WSe_2 and InSe, as indicated by the excitation paths from E_V to E_C of each layer, while an additional allowed excitation pathway arises at the Gamma-point due to the joint dispersion relations.

Fig. 2(c) and (f) compare the absorption spectra of the NbS_2/WSe_2 and InSe/WSe_2 heterostructures with those of their free-standing layers. Both vdW heterostructures exhibit high absorption coefficients (>10^5 cm^{-1}) in the ultraviolet and visible spectral ranges, arising from inherent intralayer excitations from E_V to E_C within the same material, and show notably enhanced absorption in the infrared spectral range due to

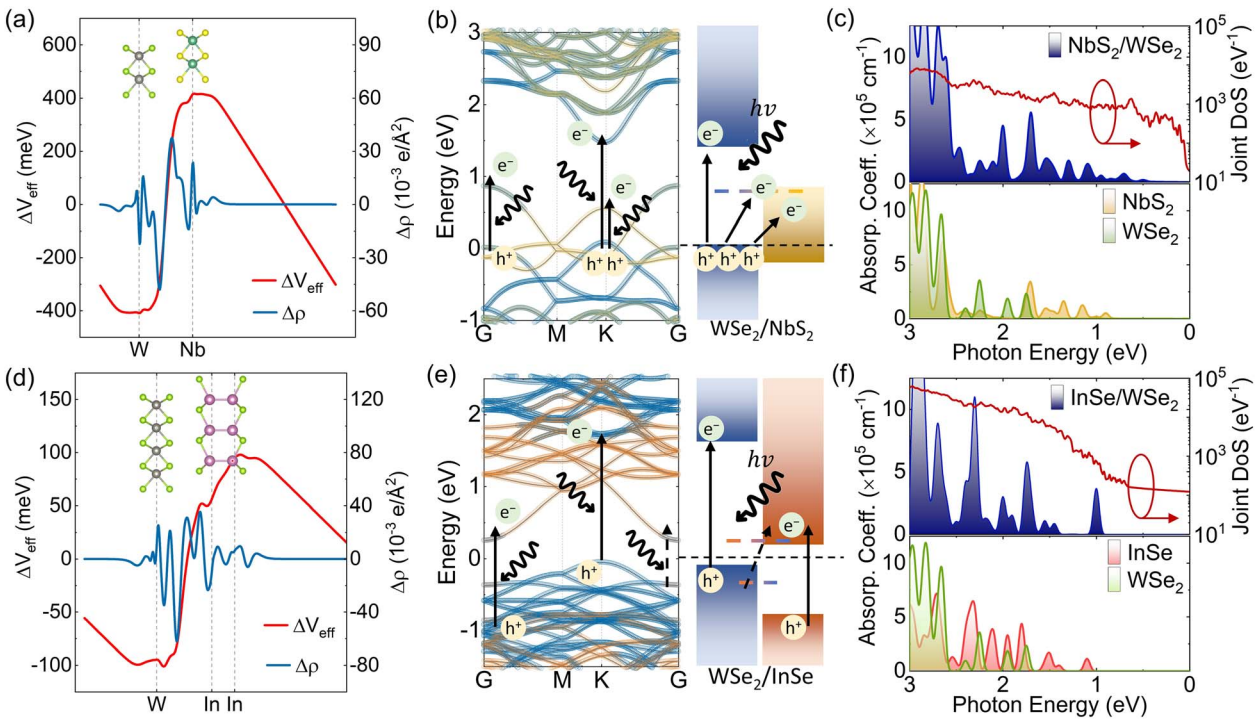

Fig. 2 (a) Effective potential variation (ΔV_{eff}) and charge redistribution ($\Delta\rho$), (b) band structure and band diagram, and (c) absorption coefficient and joint DoS for the NbS_2/WSe_2 vdW junctions. (d) Effective potential variation and charge redistribution, (e) band structure and band diagram, and (f) absorption coefficient and joint DoS for the InSe/WSe_2 vdW junctions.

allowed interlayer excitations across the layers. The computed absorption coefficients are consistent with those obtained from experimental measurements.[30,31] Notably, the $InSe/WSe_2$ heterostructure shows a threefold increase in the absorption coefficient for a photon energy of 1 eV due to the joint dispersion relations created in the vdW heterostructure. In contrast, stacking a monolayer of WSe_2 with NbS_2 enhances the absorption spectrum across the range of 0.5∼1 eV.

The absorption coefficient $\alpha(\hbar\omega)$ is calculated using a classical approach based on electronic transitions between occupied and unoccupied Kohn–Sham states.[32,33] In this framework, $\alpha(\hbar\omega)$ at photon energy $\hbar\omega$ is correlated to the joint density of states (JDoS) $\rho_{JD}(\hbar\omega)$, as given by (1),

$$\alpha(\hbar\omega) \propto |\langle k_V|H_{VC}(k)|k_C\rangle|^2 \rho_{JD}(\hbar\omega)[f(E_V) - f(E_C)], \quad (1)$$

where $H_{VC}(k)$ represents the optical transition matrix between valence band and conduction band, and $f(E)$ is the Fermi–Dirac statistics. To aid understanding, the supplementary document provides a brief outline of the primary derivation steps establishing the connection between the JDoS and the absorption coefficient. This standard formalism adequately captures the essential optical absorption properties arising from the band structure and electronic state occupation.

The divergent absorption properties stem from the distinct band alignments in the vdW heterostructures. In the NbS_2/WSe_2 heterostructure, a large built-in potential creates a broken-gap band alignment associated with significant charge redistribution that promotes substantial electron exchange and heavy doping of WSe_2. According to field emission theory, the resulting strong interfacial electric field enhances tunneling efficiency.[20] Moreover, the correlated dispersion relations increase the DoS available for interlayer excitons, promoting electron transitions from the WSe_2 valence band to the NbS_2 conduction band, and enhancing infrared photon absorption. In contrast, the staggered gap band alignment in the $InSe/WSe_2$ heterostructure leads to modest charge redistribution at the junction interface. This results in limited interlayer electron exchange and primarily enhances the DoS for interband excitations within the constituent monolayers. These results highlight that deliberate modulation of interfacial electrostatics, with transforming a staggered band alignment into a broken-gap configuration being an effective strategy, synergistically activates interlayer excitation and enhances infrared absorption in 2D vdW structures.

3 Electrostatic effects on interlayer excitation in 2D vdW heterostructures

Gate biasing has emerged as an effective strategy for modulating the electrostatics in 2D vdW heterostructures,[22–25] offering opportunities to enhance infrared absorption and broaden the photoresponse bandwidth. It's important to note that some vdW heterostructures already exhibit strong intrinsic interlayer electric fields exceeding 0.1 eV $Å^{-1}$, $InSe/WSe_2$ as an example, due to charge redistribution at the interface. In such cases, the external electric field produces only incremental changes to the band structure. To amplify the effect of external electrostatic modulation, it becomes essential to reduce interlayer coupling by using weakly interacting 2D materials and increasing the interlayer separation with an insertion layer. In this approach, the electrostatically induced potential shift at the interface is enhanced and allows for the evaluation of electric field effects. In this work, a 2D vdW heterostructure consisting of a large bandgap monolayer MoS_2 and WSe_2 was constructed, with a graphene interlayer inserted to provide weak screening and facilitate charge transfer. First-principles simulations were performed with an electric field applied in the *z*-direction that is perpendicular to the MoS_2/Graphene/WSe_2 (MGW) heterostructure to investigate the impact on interfacial electrostatics and optical absorption properties. As shown in Fig. 3(a), an electric field of 0.1 V $Å^{-1}$ (equivalent to 10 MV cm^{-1}) shifts the effective potentials of MoS_2 and WSe_2 by approximately 200 meV relative to the Fermi level. In Fig. 3(b), charge redistribution reveals that electric fields of −0.1 V $Å^{-1}$ and 0.1 V $Å^{-1}$ enhance interface dipoles at the graphene/WSe_2 and MoS_2/graphene interfaces, respectively.

Fig. 3(c) shows the absorption spectra of the MGW heterostructure. Graphene begins absorbing photons at 1 eV, while MoS_2 and WSe_2 start absorbing photons at about 1.7 eV, corresponding to the inherent absorption of the individual monolayers due to intralayer excitations from E_V to E_C, which contribute primarily to the ultraviolet and visible spectral ranges. Notably, with a positive electric field of 0.08 to 0.1 V $Å^{-1}$ (8 to 10 MV cm^{-1}), which is achievable in practical devices,[34,35] the infrared absorption coefficient has been significantly enhanced to 5×10^5 cm^{-1} for wavelengths beyond 2 μm. In contrast, a negative electric field as strong as −0.1 V $Å^{-1}$ shows a negligible impact on the optical absorption properties in the spectrum of the MGW heterostructure. The absorption threshold energies of MoS_2, WSe_2, and graphene are consistent with previously reported experimental measurements.[36–38] Notably, charge transfer from MoS_2 and WSe_2 has doped graphene and shifted its Fermi level by ΔE_F, resulting in a modified absorption threshold for interband transitions within the graphene layer. According to momentum-conserved optical transition rules, interband absorption in graphene becomes allowed only when the photon energy exceeds $2|\Delta E_F|$.[39] This doping-dependent shift in the absorption threshold in the simulated spectra shows agreement with experimental trends.

The projected band structures in Fig. 3(d) and (f) further clarify the mechanism. The dispersion relations, color-coded for MoS_2 (blue), WSe_2 (orange), and graphene (green), reveal that a positive electric field converts the staggered-gap alignment between MoS_2 and graphene into a broken-gap alignment. Such a change in band alignment induces heavy n-type doping in MoS_2 and strengthens the dipole at the graphene/WSe_2 interface, promoting low-energy interlayer excitations. As a result, electrons in the WSe_2 valence band can transition to the MoS_2 conduction band through graphene, resulting in enhanced infrared absorption. Conversely, a negative bias widens the energy gap between the WSe_2 valence band and the MoS_2 conduction band, inhibiting interlayer excitations. As such, applying an electric field that simultaneously narrows the

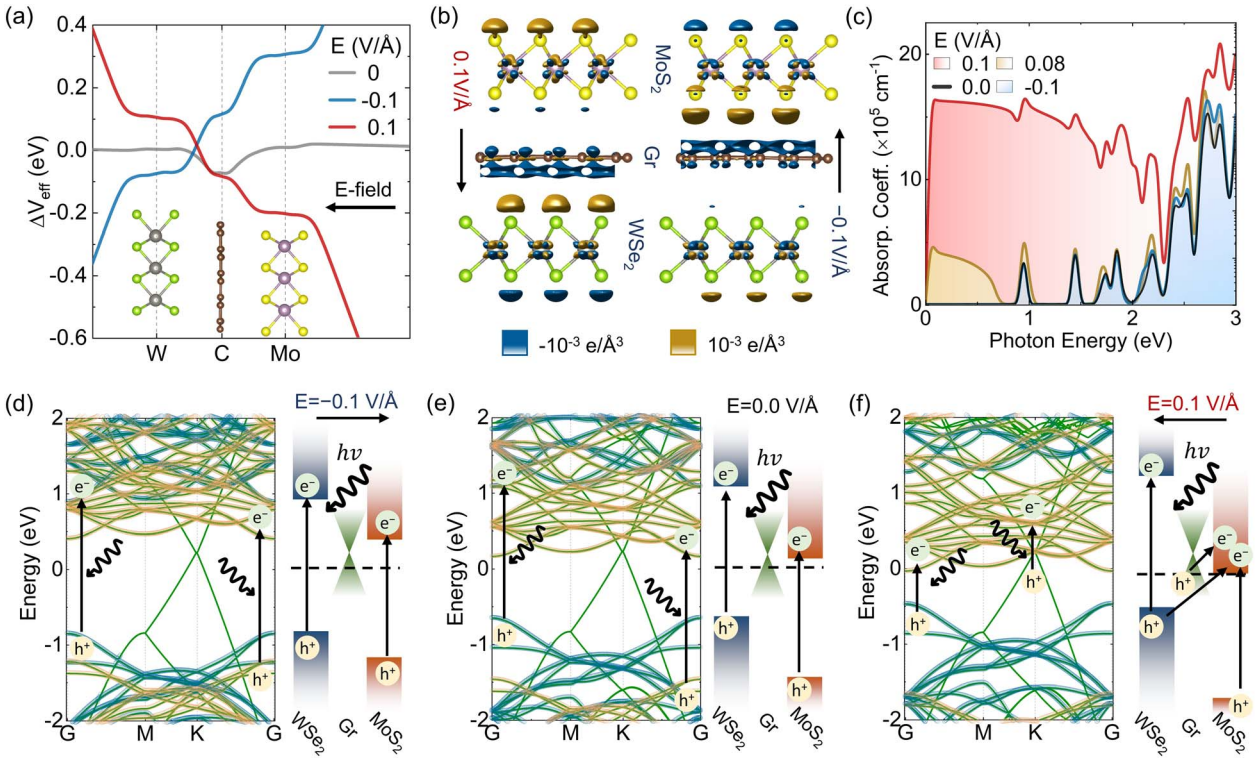

Fig. 3 (a) Effective potential variations (ΔV_{eff}) for the MoS_2/Graphene/WSe_2 (MGW) junction under electric field biases. (b) Charge redistributions ($\Delta\rho$) under electric field biases. (c) Absorption spectra of the MGW junction and corresponding band diagrams under electric fields of (d) −0.1 V $Å^{-1}$, (e) 0.0 V $Å^{-1}$, and (f) +0.1 V $Å^{-1}$.

interlayer bandgap and promotes interlayer charge transfer in 2D vdW heterostructures facilitates stronger interlayer excitations, resulting in enhanced absorption coefficients and broadened infrared spectral bandwidths. In addition, selecting 2D materials that naturally form heterostructures with smaller interlayer bandgaps may allow such effects to be achieved using lower electric fields, enabling more efficient infrared absorption through engineered band alignment. Furthermore, leveraging a positive bias to enhance infrared absorption and a negative bias to suppress unwanted carrier transitions provides a strategic pathway to enhance the spectral range and sensitivity of 2D vdW heterostructure-based photodetectors.

Beyond gate biasing, substitutional doping provides a robust alternative for generating substantial interfacial charge and inducing strong interfacial electric fields in 2D materials. This approach offers advantages such as simplifying device architecture and reducing parasitic effects.[40–43] Therefore, substitutional doping in 2D materials is regarded as a favorable technique and a key building block in the roadmap for advanced device applications.[44] Substitutional doping with Re and Fe (for n-type), and Nb, V and Ta (for p-type), which are compatible with the host lattice, has proven to be an exceptionally efficient approach for modulating charge concentrations in many 2D materials, such as MoS_2, $MoSe_2$, $MoTe_2$, and WSe_2 in their monolayer and multilayer forms.[45–48] These extensive experimental and theoretical studies have shown that substitutional doping produces stable materials and enables precise control over carrier concentrations with negligible lattice distortion, offering excellent material stability, structural compatibility, minimal defect states, and preserved band structures—features essential for engineering device-level functionality.

Fig. 4(a) illustrates the atomic structure of a vdW-stacked p–n junction comprising n-type Re-doped and p-type Nb-doped MoS_2 monolayers, each with a doping concentration of 10^{14} cm^{-2}. This doping concentration corresponds to a dopant atomic ratio of less than 2.7%, which is readily attainable through established synthesis techniques.[49,50] The doping concentrations in each layer are kept identical, and lower doping levels can be realized by increasing the size of the simulation supercell while keeping the dopant atom count fixed. Fig. 4(b) shows that an increased doping level simultaneously broadens the absorption spectral bandwidth and enhances infrared absorption, directly correlated with intensified electron exchange, as illustrated in Fig. 4(c).

To clarify the mechanism, Fig. 4(d) and (e) present a comparative analysis of the band diagrams for the doped bilayer MoS_2 p–n junction and the intrinsic bilayer MoS_2, respectively. While the undoped bilayer MoS_2 exhibits a large indirect bandgap that confines absorption to the visible and ultraviolet ranges, increased doping narrows the interlayer energy gap and intensifies electron exchange. At a doping concentration of 10^{14} cm^{-2}, a broken-gap band alignment is established, enabling absorption to extend into the far-infrared

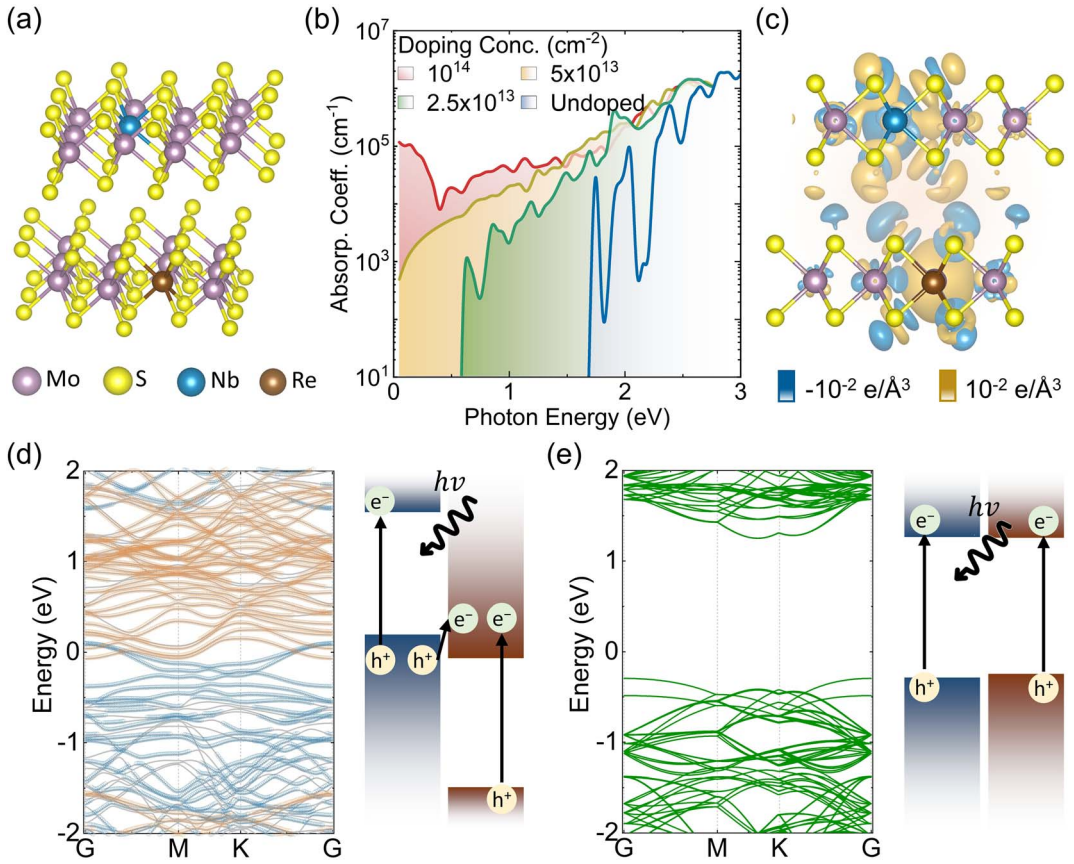

Fig. 4 (a) Atomistic structure of the bilayer MoS_2 vdW p–n homojunction. (b) Absorption spectrum of the MoS_2 p–n junction. (c) Charge redistribution ($\Delta\rho$) for the MoS_2 p–n junction compared with the intrinsic bilayer MoS_2. Band structure and band diagram for (d) the bilayer MoS_2 p–n junction and (e) the intrinsic bilayer MoS_2.

region and achieving absorption coefficients comparable to those observed in the visible and ultraviolet ranges. Notably, the enhanced infrared absorption in the bilayer MoS_2 p–n junction arises from strong interlayer charge transfer, driven by the alignment of band edges relative to the Fermi level. This mechanism offers an electrically tunable threshold for interlayer optical transitions. It is important to emphasize that achieving such tunability is inherently challenging in metal–semiconductor Schottky contacts, particularly when 2D materials are involved. In these systems, strong Fermi-level pinning at the metal–semiconductor interface constrains the alignment between the metal Fermi level and the semiconductor band edges, thereby severely limiting the effectiveness of electrostatic modulation of the band structure.

4 Conclusions

While 2D vdW heterostructures with staggered band alignment provide optical transition pathways for infrared photodetection, the efficiency has been fundamentally limited by weak interlayer coupling. This work employs first-principles simulations to demonstrate that strategic band engineering through electric field gating and substitutional doping provides effective control over band alignments in 2D vdW structures. These approaches enable simultaneous achievement of strong interlayer coupling and significantly reduced bandgaps. Systematic simulations reveal substantially enhanced absorption coefficients, in the range of 10^5 to 10^6 cm^{-1}, with broad absorption spectral tunability from ultraviolet to mid-infrared regimes, and establish a clear correlation between an enhanced infrared response and improved interlayer charge transfer. This demonstrates that such effects can be effectively modulated through the electrostatic control of band alignment. These findings provide both theoretical insights into the interlayer excitation mechanism and design principles for optimizing high-performance photodetectors in 2D material systems.

Author contributions

Zichao Ma: conceptualization, data curation, validation, methodology, writing – original draft, writing – review & editing, funding acquisition. Changjian Zhou: conceptualization, investigation, validation, supervision, writing – review & editing, funding acquisition, project administration.

Conflicts of interest

There are no conflicts to declare.

Data availability

The authors confirm that the data supporting the findings of this study are available within the article. All software mentioned in the text is used in its official release version.

Supplementary information is available: the band structures of 2D monolayers and heterojunctions computed using HSE06 hybrid functional, the periodic boundary condition setups, and the basic theory of JDoS and absorption. See DOI: **https://doi.org/10.1039/d5na00648a**.

Acknowledgements

This research was funded by the National Natural Science Foundation of China (No. 62574084), the Guangdong Provincial Key Field Research and Development Program (2022B0701180002), the Guangdong Basic and Applied Basic Research Foundation (2025A1515010391), and the Guangzhou Science and Technology Program (SL2024A04J3755). The authors gratefully acknowledge HZWTECH for providing computational facilities. The authors also acknowledges the support of the Micro & Nano Electronics Platform (MNEP) at the South China University of Technology for providing fabrication, characterization, and computation resources.

References

1 C. Schneider, M. M. Glazov, T. Korn, S. Höfling and B. Urbaszek, *Nat. Commun.*, 2018, **9**, 2695.
2 J. Yao and G. Yang, *Nanoscale*, 2020, **12**, 454–476.
3 L. Tao, Z. Chen, Z. Li, J. Wang, X. Xu and J.-B. Xu, *InfoMat*, 2021, **3**, 36–60.
4 C.-H. Lee, G.-H. Lee, A. M. van der Zande, W. Chen, Y. Li, M. Han, X. Cui, G. Arefe, C. Nuckolls, T. F. Heinz, J. Guo, J. Hone and P. Kim, *Nat. Nanotechnol.*, 2014, **9**, 676–681.
5 G. H. Shin, C. Park, K. J. Lee, H. J. Jin and S.-Y. Choi, *Nano Lett.*, 2020, **20**, 5741–5748.
6 H. Shang, F. Gao, M. Dai, Y. Hu, S. Wang, B. Xu, P. Wang, B. Gao, J. Zhang and P. Hu, *Small Methods*, 2023, **7**, 2200966.
7 C. Zhou, S. Zhang, Z. Lv, Z. Ma, C. Yu, Z. Feng and M. Chan, *npj 2D Mater. Appl.*, 2020, **4**, 46.
8 S. Lukman, L. Ding, L. Xu, Y. Tao, A. C. Riis-Jensen, G. Zhang, Q. Y. S. Wu, M. Yang, S. Luo, C. Hsu, L. Yao, G. Liang, H. Lin, Y.-W. Zhang, K. S. Thygesen, Q. J. Wang, Y. Feng and J. Teng, *Nat. Nanotechnol.*, 2020, **15**, 675–682.
9 K. Choudhary, K. F. Garrity, S. T. Hartman, G. Pilania and F. Tavazza, *Phys. Rev. Mater.*, 2023, **7**, 14009.
10 T. Mueller and E. Malic, *npj 2D Mater. Appl.*, 2018, **2**, 29.
11 V. R. Policht, H. Mittenzwey, O. Dogadov, M. Katzer, A. Villa, Q. Li, B. Kaiser, A. M. Ross, F. Scotognella, X. Zhu, A. Knorr, M. Selig, G. Cerullo and S. Dal Conte, *Nat. Commun.*, 2023, **14**, 7273.
12 J. Kistner-Morris, A. Shi, E. Liu, T. Arp, F. Farahmand, T. Taniguchi, K. Watanabe, V. Aji, C. H. Lui and N. Gabor, *Nat. Commun.*, 2024, **15**, 4075.
13 O. Karni, E. Barré, V. Pareek, J. D. Georgaras, M. K. L. Man, C. Sahoo, D. R. Bacon, X. Zhu, H. B. Ribeiro, A. L. O'Beirne, J. Hu, A. Al-Mahboob, M. M. M. Abdelrasoul, N. S. Chan, A. Karmakar, A. J. Winchester, B. Kim, K. Watanabe, T. Taniguchi, K. Barmak, J. Madéo, F. H. da Jornada, T. F. Heinz and K. M. Dani, *Nature*, 2022, **603**, 247–252.
14 S. Das, Y. Wang, Y. Dai, S. Li and Z. Sun, *Light:Sci. Appl.*, 2021, **10**, 27.
15 M. Son, H. Jang, D.-B. Seo, J. H. Lee, J. Kim, M. Kim, S. Kang, S. Yim, W. Song, J.-W. Yoo, H. Y. Kim, S. S. Lee and K.-S. An, *Adv. Funct. Mater.*, 2024, **34**, 2308906.
16 M. Long, E. Liu, P. Wang, A. Gao, H. Xia, W. Luo, B. Wang, J. Zeng, Y. Fu, K. Xu, W. Zhou, Y. Lv, S. Yao, M. Lu, Y. Chen, Z. Ni, Y. You, X. Zhang, S. Qin, Y. Shi, W. Hu, D. Xing and F. Miao, *Nano Lett.*, 2016, **16**, 2254–2259.
17 C. Zhang, C. Gong, Y. Nie, K.-A. Min, C. Liang, Y. J. Oh, H. Zhang, W. Wang, S. Hong, L. Colombo, R. M. Wallace and K. Cho, *2d Mater*, 2017, **4**, 015026.
18 S. Ovesen, S. Brem, C. Linderälv, M. Kuisma, T. Korn, P. Erhart, M. Selig and E. Malic, *Commun. Phys.*, 2019, **2**, 23.
19 F. Wu, T. Lovorn and A. H. MacDonald, *Phys. Rev. Lett.*, 2017, **118**, 147401.
20 W. J. Yu, Q. A. Vu, H. Oh, H. G. Nam, H. Zhou, S. Cha, J.-Y. Kim, A. Carvalho, M. Jeong, H. Choi, A. H. Castro Neto, Y. H. Lee and X. Duan, *Nat. Commun.*, 2016, **7**, 13278.
21 H. Wu, N. Li, M. Tang, W. Tang and J. Zhao, *ACS Appl. Nano Mater.*, 2023, **6**, 22711–22719.
22 V. K. Dat, C. Hong, M. D. Tran, T. K. Chau, V. D. Do, T. T. Tran, M. C. Nguyen, H. P. Duong, S. Oh, W. J. Yu, J. Kim and J.-H. Kim, *Adv. Electron. Mater.*, 2024, **10**, 2300517.
23 H. Wang, Y. Li, P. Gao, J. Wang, X. Meng, Y. Hu, J. Yang, Z. Huang, W. Gao, Z. Zheng, Z. Wei, J. Li and N. Huo, *Adv. Mater.*, 2024, **36**, 2309371.
24 D. Shen, H. Yang, T. Patel, D. A. Rhodes, T. Timusk, Y. N. Zhou, N. Y. Kim and A. W. Tsen, *ACS Nano*, 2024, **18**, 11193–11199.
25 C. Chen, X. Lu, B. Deng, X. Chen, Q. Guo, C. Li, C. Ma, S. Yuan, E. Sung, K. Watanabe, T. Taniguchi, L. Yang and F. Xia, *Sci. Adv.*, 2020, **6**, eaay6134.
26 M.-H. Chiu, C. Zhang, H.-W. Shiu, C.-P. Chuu, C.-H. Chen, C.-Y. S. Chang, C.-H. Chen, M.-Y. Chou, C.-K. Shih and L.-J. Li, *Nat. Commun.*, 2015, **6**, 7666.
27 W. Shan, A. Shi, Z. Xin, X. Zhang, B. Wang, Y. Li and X. Niu, *Adv. Funct. Mater.*, 2025, **35**, 2412773.
28 S. Vaziri, E. Yalon, M. Muñoz Rojo, S. V. Suryavanshi, H. Zhang, C. J. McClellan, C. S. Bailey, K. K. H. Smithe, A. J. Gabourie, V. Chen, S. Deshmukh, L. Bendersky, A. V. Davydov and E. Pop, *Sci. Adv.*, 2019, **5**, eaax1325.
29 J. Taylor, H. Guo and J. Wang, *Phys. Rev. B:Condens. Matter Mater. Phys.*, 2001, **63**, 245407.
30 J. Y. Kwak, *Results Phys.*, 2019, **13**, 102202.
31 X. Sun, B. Shi, H. Wang, N. Lin, S. Liu, K. Yang, B. Zhang and J. He, *Adv. Opt. Mater.*, 2020, **8**, 1901181.
32 N. T. Han, W. Bang-Li, K.-I. Lin, V. K. Dien and M.-F. Lin, *RSC Adv.*, 2022, **12**, 32674–32683.
33 L. Matthes, O. Pulci and F. Bechstedt, *New J. Phys.*, 2014, **16**, 105007.

34 G. V Resta, Y. Balaji, D. Lin, I. P. Radu, F. Catthoor, P.-E. Gaillardon and G. De Micheli, *ACS Nano*, 2018, **12**, 7039–7047.
35 Z. Ma, C. Prawoto, Z. Ahmed, Y. Xiao, L. Zhang, C. Zhou and M. Chan, *J. Mater. Chem. C*, 2019, **7**, 6273–6278.
36 H. Fang, C. Battaglia, C. Carraro, S. Nemsak, B. Ozdol, J. S. Kang, H. A. Bechtel, S. B. Desai, F. Kronast, A. A. Unal, G. Conti, C. Conlon, G. K. Palsson, M. C. Martin, A. M. Minor, C. S. Fadley, E. Yablonovitch, R. Maboudian and A. Javey, *Proc. Natl. Acad. Sci. U. S. A.*, 2014, **111**, 6198–6202.
37 J. S. Ross, P. Rivera, J. Schaibley, E. Lee-Wong, H. Yu, T. Taniguchi, K. Watanabe, J. Yan, D. Mandrus, D. Cobden, W. Yao and X. Xu, *Nano Lett.*, 2017, **17**, 638–643.
38 K. F. Mak, L. Ju, F. Wang and T. F. Heinz, *Solid State Commun.*, 2012, **152**, 1341–1349.
39 H. Yan, F. Xia, W. Zhu, M. Freitag, C. Dimitrakopoulos, A. A. Bol, G. Tulevski and P. Avouris, *ACS Nano*, 2011, **5**, 9854–9860.
40 V. T. Vu, T. L. Phan, T. T. H. Vu, M. H. Park, V. D. Do, V. Q. Bui, K. Kim, Y. H. Lee and W. J. Yu, *ACS Nano*, 2022, **16**, 12073–12082.
41 Z. Ma, L. Zhang and M. Chan, *IEEE Electron Device Lett.*, 2025, **46**, 1385–1388.
42 R. Wen, Z. Ma, Y. Luo and C. Zhou, *Phys. Rev. Appl.*, 2025, **23**, 064010.
43 Z. Ma, L. Zhang, C. Zhou and M. Chan, *IEEE Electron Device Lett.*, 2021, **42**, 343–346.
44 D. Akinwande, C. Huyghebaert, C.-H. Wang, M. I. Serna, S. Goossens, L.-J. Li, H.-S. P. Wong and F. H. L. Koppens, *Nature*, 2019, **573**, 507–518.
45 Y. Pan, T. Jian, P. Gu, Y. Song, Q. Wang, B. Han, Y. Ran, Z. Pan, Y. Li, W. Xu, P. Gao, C. Zhang, J. He, X. Xu and Y. Ye, *Nat. Commun.*, 2024, **15**, 9631.
46 H. Li, M. Cheng, P. Wang, R. Du, L. Song, J. He and J. Shi, *Adv. Mater.*, 2022, **34**, 2200885.
47 M. Das, D. Sen, N. U. Sakib, H. Ravichandran, Y. Sun, Z. Zhang, S. Ghosh, P. Venkatram, S. Subbulakshmi Radhakrishnan, A. Sredenschek, Z. Yu, K. J. Sarkar, M. U. K. Sadaf, K. Meganathan, A. Pannone, Y. Han, D. E. Sanchez, D. Somvanshi, Z. Sofer, M. Terrones, Y. Yang and S. Das, *Nat. Electron.*, 2024, **8**, 24–35.
48 Z. Ma, C. J. Estrada, K. Gong, L. Zhang and M. Chan, *Adv. Electron. Mater.*, 2022, **8**, 2200480.
49 M. Okada, N. Nagamura, T. Matsumura, Y. Ando, A. K. A. Lu, N. Okada, W.-H. Chang, T. Nakanishi, T. Shimizu, T. Kubo, T. Irisawa and T. Yamada, *APL Mater.*, 2021, **9**, 121115.
50 W. Li, J. Huang, B. Han, C. Xie, X. Huang, K. Tian, Y. Zeng, Z. Zhao, P. Gao, Y. Zhang, T. Yang, Z. Zhang, S. Sun and Y. Hou, *Advanced Science*, 2020, **7**, 2001080.